ADVANCED FUNCTIONAL MATERIALS
www.afm-journal.de

Visualizing Energy Transfer at Buried Interfaces in Layered Materials Using Picosecond X-Rays

*Clara Nyby, Aditya Sood, Peter Zalden, Alexander J. Gabourie, Philipp Muscher, Daniel Rhodes, Ehren Mannebach, Jeff Corbett, Apurva Mehta, Eric Pop, Tony F. Heinz, and Aaron M. Lindenberg**

Understanding the fundamentals of nanoscale heat propagation is crucial for next-generation electronics. For instance, weak van der Waals bonds of layered materials are known to limit their thermal boundary conductance (TBC), presenting a heat dissipation bottleneck. Here, a new nondestructive method is presented to probe heat transport in nanoscale crystalline materials using time-resolved X-ray measurements of photoinduced thermal strain. This technique directly monitors time-dependent temperature changes in the crystal and the subsequent relaxation across buried interfaces by measuring changes in the *c*-axis lattice spacing after optical excitation. Films of five different layered transition metal dichalcogenides MoX_2 [X = S, Se, and Te] and WX_2 [X = S and Se] as well as graphite and a W-doped alloy of $MoTe_2$ are investigated. TBC values in the range 10–30 MW m^{-2} K^{-1} are found, on *c*-plane sapphire substrates at room temperature. In conjunction with molecular dynamics simulations, it is shown that the high thermal resistances are a consequence of weak interfacial van der Waals bonding and low phonon irradiance. This work paves the way for an improved understanding of thermal bottlenecks in emerging 3D heterogeneously integrated technologies.

1. Introduction

Heat dissipation presents a significant bottleneck for the performance of numerous computing, optoelectronic, and energy storage technologies.[1–5] Understanding thermal energy transport across various interfaces which appear in heterogeneous systems remains a key challenge.[6] Experimentally, the study of thermal boundary conductance (TBC) between two dissimilar materials is typically carried out in specially designed model systems where the interface of interest is positioned close (≈few nanometers) to the surface of the sample.[7–9] However, these model systems often cannot incorporate the complexity of real devices, where thermal bottlenecks frequently occur at buried interfaces, which could be at depths of tens to hundreds of nanometers up to several micrometers.[10] With the advent of 3D integrated circuits,[11] where heat dissipation could be a major issue, it is of paramount importance to develop nondestructive thermal metrologies for buried interfaces and in spatially confined geometries.

Developing such metrologies is particularly relevant for van der Waals (vdW) layered materials such as transition metal dichalcogenides (TMDs), which are promising candidates for next-generation applications in optoelectronics and photonics. Because the weak vdW bonding in these materials limits thermal conduction, heat management is a key consideration for integrating

C. Nyby
Department of Chemistry
Stanford University
Stanford, CA 94305, USA

Dr. A. Sood, Prof. T. F. Heinz, Prof. A. M. Lindenberg
Stanford Institute for Materials and Energy Sciences
SLAC National Accelerator Laboratory
Menlo Park, CA 94025, USA
E-mail: aaronl@stanford.edu

Dr. P. Zalden
European XFEL
Holzkoppel 4, Schenefeld 22869, Germany

A. J. Gabourie, Prof. E. Pop
Department of Electrical Engineering
Stanford University
Stanford, CA 94305, USA

P. Muscher, Dr. E. Mannebach, Prof. A. M. Lindenberg
Department of Materials Science and Engineering
Stanford University
Stanford, CA 94305, USA

Prof. D. Rhodes
Department of Materials Science and Engineering
University of Wisconsin–Madison
Madison, WI 53706, USA

Dr. J. Corbett, Dr. A. Mehta
Stanford Synchrotron Radiation Lightsource
SLAC National Accelerator Laboratory
Menlo Park, CA 94025, USA

Prof. T. F. Heinz
Department of Applied Physics
Stanford University
Stanford, CA 94305, USA

The ORCID identification number(s) for the author(s) of this article can be found under https://doi.org/10.1002/adfm.202002282.

DOI: 10.1002/adfm.202002282

them into devices.[2,12,13] Directly observing heat transport at buried interfaces is especially difficult in these materials due to their low out-of-plane (i.e., parallel to the *c*-axis) thermal conductivity.[14] Widely used methods such as time-domain thermoreflectance (TDTR)[7] and frequency-domain thermoreflectance (FDTR)[15] are ideal for measuring thermal transport at the interface between a metal transducer and substrate or at interfaces below very thin layers of material. However, probing buried interfaces is challenging due to the competing effects of various thermal impedances in the network. Similar difficulties are faced by electrothermal techniques like the 3ω method,[16] where buried TBC measurements must deconvolve the effect of heat transport across the film thickness. An additional drawback of both the optical and electrothermal methods is the requirement of fabricating metal electrodes, which introduce additional uncertainty from the metal-film TBC. Raman thermometry has been demonstrated to be a useful technique to nondestructively measure TBC in atomically thin materials,[8,17] including recently at buried TMD interfaces.[18] However, it typically requires that the upper layers are sufficiently transparent, and the buried layers have sufficiently large temperature-dependent changes in Raman peak position and well-characterized optical absorption, or a prominent Stokes/anti-Stokes ratio.

In contrast to optical and electrothermal methods, X-rays offer unique advantages in terms of both material specificity and depth of penetration (e.g., ≈500 µm in silicon at 15 keV). Here, we report a new technique for observing thermal energy dissipation at buried interfaces in nanoscale vdW-layered crystals using optical pump, picosecond X-ray diffraction (XRD) probe measurements. This method leverages the high sensitivity of X-rays to detect extremely small thermally induced strains at the 10^{-7} level.[19,20] The need for a transducer layer is avoided by directly exciting the layered crystal. As the material cools, we measure its time-dependent *c*-axis strain. Finite-element (FE) simulations are used to model this combined optical and thermal process to extract the TBC with the substrate, to which these measurements are uniquely sensitive. Using this approach, we measure TBCs of five TMD layered crystals (MoX_2 where X = S, Se, Te, and WX_2, where X = S and Se), graphite and W-doped alloy of $MoTe_2$ ($Mo_{0.93}W_{0.07}Te_2$) on *c*-plane sapphire (Al_2O_3) substrates. Notably, most of the measured TBC values lie in the range 10–30 MW m^{-2} K^{-1} at room temperature, which is at least one order of magnitude lower than typical metal–dielectric interfaces used in the semiconductor industry. We explain this thermal bottleneck effect in terms of the low phonon irradiance of layered materials and weak vdW bonding to the substrate. This work demonstrates the suitability of picosecond XRD to probe interfacial coupling in isolated layered crystals and underscores the importance of TBC in determining the ultimate performance of 2D material-based devices.

2. Results and Discussion

Measurements were conducted at the Stanford Synchrotron Radiation Lightsource (SSRL) beamline 10–2 using monochromatized and focused (≈300 µm full width at half maximum or FWHM) 15 keV X-rays to probe isolated single crystals (see **Figure 1**a) on the sapphire substrates. The time resolution of the measurements is limited by the 60 ps FWHM pulse length of the probe X-rays. We synchronize a femtosecond 1030 nm fiber laser with a 1.28 MHz repetition rate and 2.6 W average power to the electron bunch radio-frequency (RF) signal and use a barium borate crystal to generate a 515 nm pump pulse with an FWHM of 500 fs. The spot size of the optical pump is ≈1 mm FWHM, larger than both the lateral size of the samples (10–100 µm) and the spot size of the X-rays (≈300 µm FWHM), to ensure homogeneous excitation. To achieve pump–probe spatial overlap, the TMD (or graphite) crystal is placed at the center of rotation of a six-circle diffractometer, and the pump beam is directed to the sample with a half-circle mirror such that the pump and probe beams are nearly collinear, with a crossing angle of ≈1°. Diffracted X-rays from the (008) reflection of the TMD (or graphite) crystals are captured with a Pilatus 100K detector mounted 950 mm from the sample.

We measure the dynamic photoinduced strain response in the thin crystal by measuring center-of-mass changes in the diffraction images. Previous work discusses in detail how the strain response is extracted from center-of-mass changes in Bragg reflections.[19] Strain is linearly related to temperature rise via the coefficient of thermal expansion. As the sample cools due to thermal transport across the sample–substrate interface, the time-dependent strain provides a direct measurement of the normalized cooling curve on a nanosecond timescale (see Figure 1b–d). We note that this approach does not rely on an absolute measurement of temperature, only its rate of change, similar to ultrafast thermoreflectance techniques. The thickness of the flakes, measured by atomic force microscopy, ranges from 30 to 360 nm (see the Supporting Information). Note that because the X-ray penetration depth (e.g., ≈100 µm for MoS_2 at 15 keV) is orders of magnitude larger than the film thickness, the change in the center-of-mass of the Bragg peak provides the thickness-averaged strain. We extract the TBC values using an FE model that calculates the full depth- and time-dependent temperature profile, as described below.

The time-dependent interlayer strain (i.e., parallel to the *c*-axis), η, in a 200 nm thick MoS_2 sample is shown in Figure 1c. The negative strain following time zero corresponds to a contraction of the lattice caused by a photoinduced modulation of the vdW forces between the layers.[21] Following this transient effect near zero delay time, fitting the longer time strain relaxation dynamics to a single exponential function yields cooling time constants ranging from 13 to 70 ns for the various thicknesses of MoS_2. Assuming a 1D diffusion model as described earlier,[22] this time constant τ can be directly related to the TBC as, $\tau = C_v l/G$, where l is the thickness of the flake, C_v is the volumetric specific heat of the sample, and G is the TBC with the substrate. For the thinnest MoS_2 crystal (l = 33 nm), this simple model estimates G = 5.3 MW m^{-2} K^{-1}, in rough agreement with the value extracted using the more detailed FE model described below.

The normalized temperature profile is fit to an FE heat diffusion model to extract the TBC at the interface between the layered crystal and sapphire substrate. Other input parameters for this simulation are the thickness, volumetric specific heat, optical attenuation coefficient (α), and out-of-plane thermal

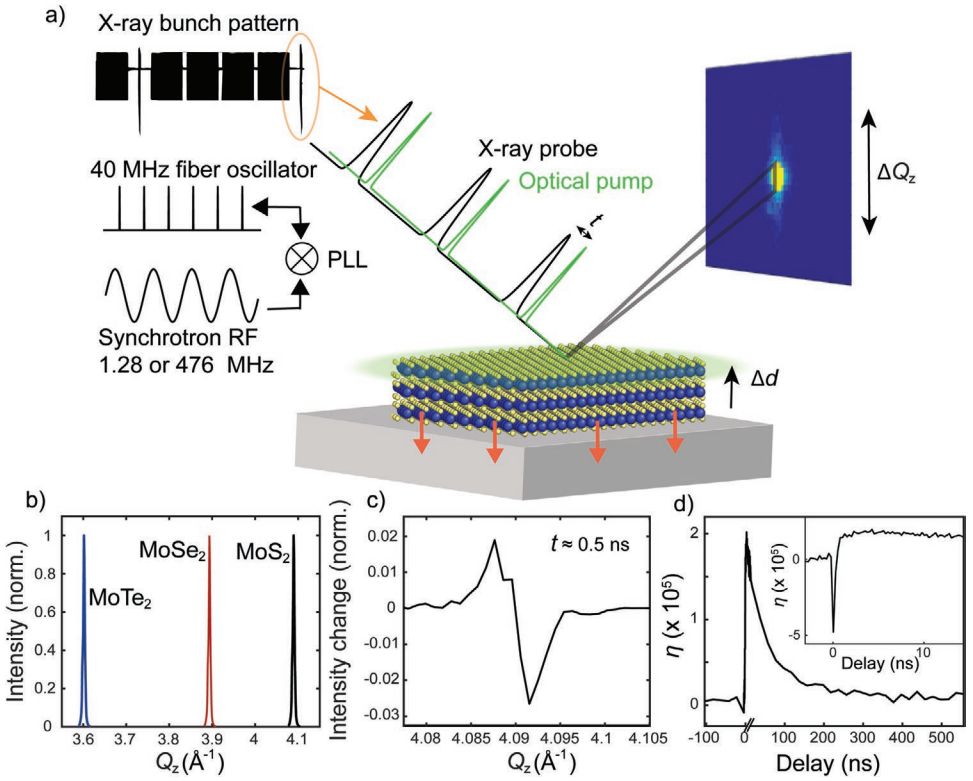

Figure 1. a) Experimental setup of time-resolved X-ray diffraction (XRD) probing out-of-plane lattice reflections, where Δd indicates a change in lattice spacing, ΔQ_z is the change in reciprocal lattice, and t is the time delay between pump (800 nm) and probe (X-ray) pulses. A 40 MHz oscillator is synchronized to the synchrotron radio frequency (RF) at 1.28 or 476 MHz via a phase-locked loop (PLL), and the timing of the laser pulse is controlled with electronic delays. An electronically gated detector captures X-rays in a single 10 mA pulse, separated from other pulse trains by ≈60 ns. b) Normalized intensity profile of a 33 nm thick MoS_2 crystal (008) Bragg reflection, compared to the (008) reflections in $MoSe_2$ and $MoTe_2$ using 15 keV X-rays. c) The change in intensity after time zero ($t \approx 0.5$ ns) of the MoS_2 intensity in (a), showing the center-of-mass change. d) Strain response, η, of a 200 nm thick MoS_2 crystal extracted from center-of-mass changes in the (008) Bragg reflection. The inset shows the shorter time response.

conductivity of the layered material (κ_z), as well as C_v and κ_z of the substrate. Heat conduction is modeled as 1D since the pump laser spot size is larger than the lateral dimensions of the isolated single crystals. The governing equations used to model the heat transfer are

$$C_v \frac{\partial T}{\partial t} - \kappa_z \frac{\partial^2 T}{\partial z^2} = q \tag{1}$$

where $q = q_0 \exp(-\alpha z)$ is the heat deposited per unit volume by the laser pulse in the film over the optical absorption depth $L_p = 1/\alpha$. The sapphire substrate is transparent to the pump wavelength and does not absorb any energy directly from the laser pulse, i.e., $q = 0$ in the substrate. Literature values for L_p and C_v are listed in Table S1 (Supporting Information) for all the materials. A thermal boundary conductance G is included at the interface between the film and sapphire substrate and is modeled by

$$-\kappa_{z,t} \left.\frac{\partial T}{\partial z}\right|_t = -\kappa_{z,b} \left.\frac{\partial T}{\partial z}\right|_b = G(T_t - T_b) \tag{2}$$

where T_t and T_b are the top and bottom temperatures across the interface. Because the temperature jumps do not exceed 5 K, thermal radiation is ignored. The substrate in the simulation is much thicker (100 µm) than the films (up to 360 nm) and therefore acts as a heat sink with close to infinite capacity.

Previous studies have shown that vdW layered materials can exhibit significant thermal size effects in the out-of-plane direction,[23] i.e., κ_z decreases for films thinner than ≈1 µm, even at room temperature. For example, $\kappa_z \approx 0.9$ W m^{-1} K^{-1} across a 20 nm thick MoS_2 film, which is ≈5× lower than the bulk value of ≈5 W m^{-1} K^{-1}.[23] This is due to the long mean-free-paths (MFPs) of c-axis thermal phonons, which scatter diffusely at the interfaces. This has also been seen in first principles calculations of MoS_2,[24] WS_2, and WSe_2.[25] To account for size effects in MoS_2, WS_2, and WSe_2, we use a Boltzmann transport equation (BTE)-based suppression function in conjunction with the ab initio MFP calculations to determine κ_z as a function of thickness.[23] For graphite, we use previous thin-film measurements made using TDTR.[26] For $MoSe_2$, $MoTe_2$, and $Mo_{1-x}W_xTe_2$ ($x = 0.07$), we assume that the normalized MFP accumulation functions are similar to MoS_2 and estimate κ_z for the thin films by scaling with the ratio of their bulk κ_z values.[25,27] Table S1 (Supporting Information) lists κ_z for each sample, following the procedure outlined above.

Figure 2 shows the temperature rise as a function of z and t for two thicknesses of MoS_2. We find that the film equilibrates internally before a significant amount of heat has left it, so that only the TBC of the MoS_2/Al_2O_3 interface determines the rate

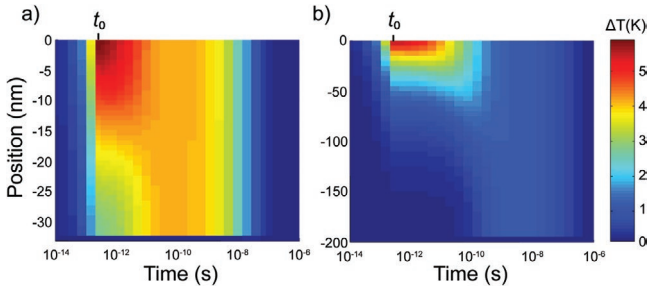

Figure 2. Finite-element simulations of heat propagation across MoS_2. Simulated time-dependent temperature rise in a) 33 nm thick flake and b) 200 nm flake as a function of depth in the sample. A ≈500 fs laser pulse is incident on the sample at the time point indicated by t_0.

of cooling. Because of this, the simulations are largely insensitive to κ_z of the film. To fit the experimental data, from the FE simulations, we evaluate the time-dependent temperature rise averaged across the film thickness. Thickness averaging is performed because the penetration depth of the 15 keV X-rays is several orders of magnitude larger than the film thickness, as noted above. Representative data and model best fits for the various materials are shown in **Figure 3**. For example, for MoS_2 samples of thickness 33–200 nm, we estimated a TBC between 8 and 28 MW m^{-2} K^{-1} with sapphire, at room temperature. Error bars are calculated by propagating uncertainties of ±5% in thickness, ±10% in volumetric specific heat, ±10% in penetration depth, and ±2 ns in determination of time zero, and adding the individual contributions in quadrature. All reported values are summarized in **Table 1** and plotted in the Supporting Information.

We find that the TBCs for MoS_2/sapphire lie within the range of previously reported values for MoS_2/SiO_2 measured using TDTR[23] and Raman thermometry,[8,13] as well as junctions between different layered materials[17,18] (see **Figure 4**a). In general, we do not observe a systematic dependence of TBC on film thickness. This is as expected, since to first order, the TBC is related to the heat capacity and phonon group velocity, and neither of these quantities depends on thickness. While there is some variation in the measured values, they lie largely in the range 10–30 MW m^{-2} K^{-1} (see Table 1) and are significantly lower than most metal/Al_2O_3 interfaces measured previously (see Figure 4b and Table S3 in the Supporting Information). These junctions can therefore create a significant bottleneck for heat dissipation in TMD-based devices. For example, a single, atomically sharp vdW junction with a TBC of 10 MW m^{-2} K^{-1} has the same thermal resistance as a film of ≈140 nm of amorphous SiO_2 (also known as the Kapitza length).

To gain insight into the physics of interfacial transport, we compute the TBC at the MoS_2/sapphire interface using molecular dynamics (MD) simulations in the bulk and monolayer limit. For bulk MoS_2, we use a nonequilibrium MD (NEMD) method to extract the TBC. We apply a temperature gradient across an MoS_2/sapphire structure until a steady-state heat current has been achieved. The resulting temperature profile, averaged over ten independent simulations, as well as the corresponding structure can be seen in Figure 4c. Using Fourier's law, we compute the TBC for bulk MoS_2 on crystalline Al_2O_3 to

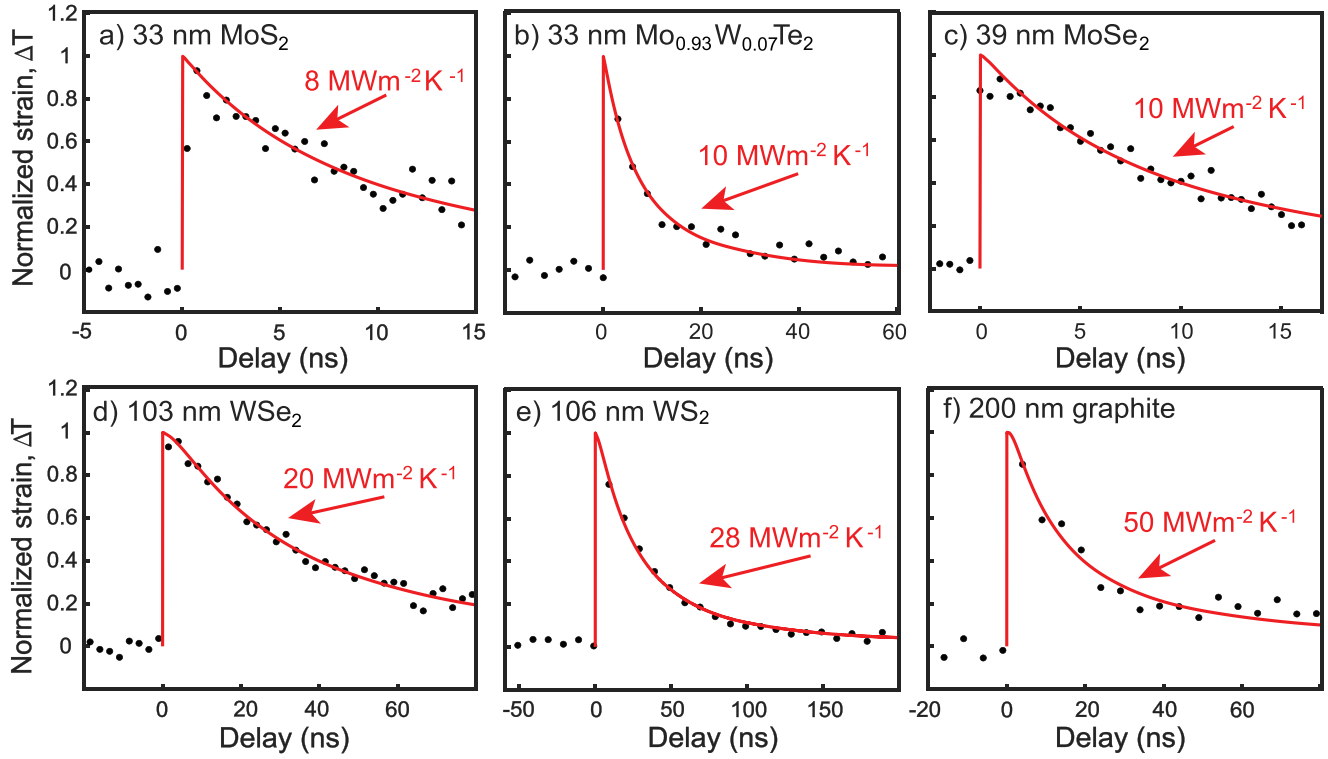

Figure 3. Time-resolved strain response measurements (symbols) of a) 33 nm thick MoS_2, b) 33 nm $Mo_{0.93}W_{0.07}Te_2$, c) 39 nm $MoSe_2$, d) 103 nm WSe_2, e) 106 nm WS_2, and f) 200 nm graphite crystals, overlaid with best-fit simulation results (red lines). Additional data and analyses are provided in Figures S4–S10 in the Supporting Information.

Table 1. Summary of measured TBC values. All samples are on sapphire, at room temperature.

Material	Thickness [nm]	G [MW m^{-2} K^{-1}]
MoS_2	33	8 ± 1.2
	43	18 ± 3.5
	52	28 ± 3.3
	130	20 ± 2.2
	200	20 ± 2.5
$MoSe_2$	39	10 ± 1.2
$MoTe_2$	30	9 ± 1.3
	360	32 ± 3.6
WSe_2	103	20 ± 2.2
	185	28 ± 3.2
WS_2	106	28 ± 3.3
$Mo_{0.93}W_{0.07}Te_2$	33	10 ± 1.6
	156	50 ± 5.6
Graphite	200	50 ± 10

be 18.6 ± 0.8 MW m^{-2} K^{-1} at room temperature, which agrees well with our range of measured values (8–28 MW m^{-2} K^{-1}) shown in Figure 4a.

To calculate the TBC of monolayer MoS_2 on sapphire, we employ the approach-to-equilibrium molecular dynamics (AEMD) method used recently.[28] We first heat MoS_2 to 500 K and set the sapphire to 300 K, then release the temperature constraints. During the temperature equilibration process (see Figure 4d), we monitor the temperature of both MoS_2 and sapphire, which can be used in an equivalent thermal circuit[28] (see Figure S2a in the Supporting Information) to compute the TBC. The extracted TBC for monolayer MoS_2 on crystalline Al_2O_3 is 15.3 ± 0.3 MW m^{-2} K^{-1}, similar to that computed for bulk MoS_2 using NEMD, suggesting that TBC has a weak dependence on the number of layers. We also compute the TBC between monolayer MoS_2 and amorphous Al_2O_3 (see the inset of Figure 4d) which gives 18.9 ± 0.5 MW m^{-2} K^{-1}. Interestingly, this is slightly higher than the TBC of monolayer MoS_2 on crystalline Al_2O_3. We suggest that this is due to the broader density of states in the amorphous substrate that overlaps better with the MoS_2, causing improved interfacial heat transfer.[29] These insights could be beneficial for the design of substrates for 2D

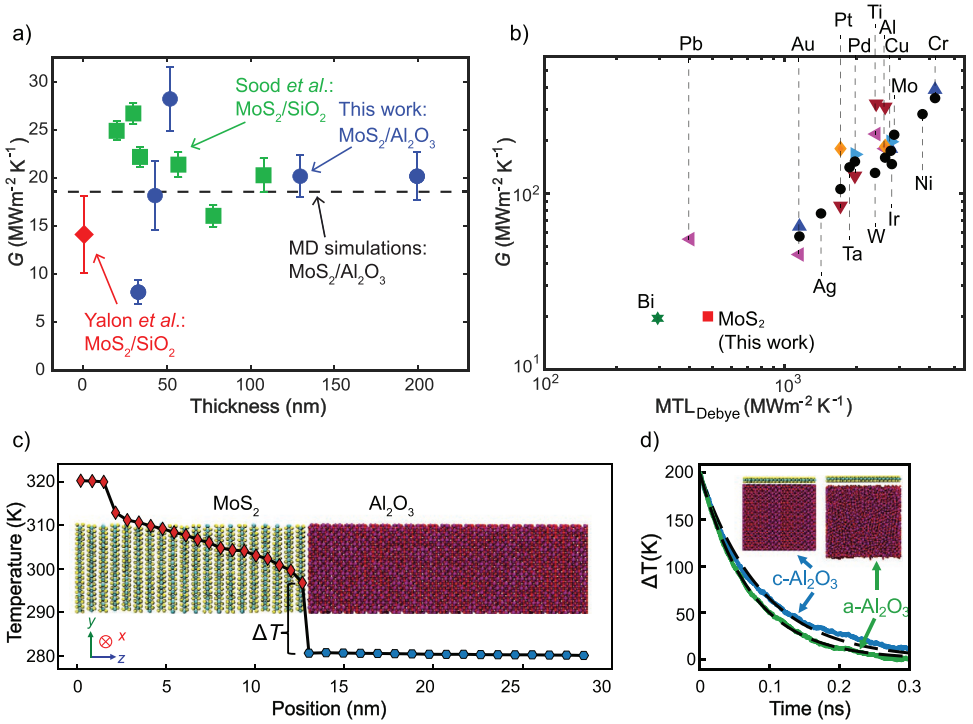

Figure 4. a) Values of thermal boundary conductance, G, for MoS_2 on sapphire compared to previously reported values in monolayer (red diamond)[8,13] and thin films (green squares)[23] on SiO_2/Si substrates using Raman thermometry and time-domain thermoreflectance, respectively. The dashed horizontal line corresponds to the TBC calculated by nonequilibrium molecular dynamics simulations for bulk MoS_2 on sapphire, 18.6 MW m^{-2} K^{-1}. b) Average of all measurements of TBC for MoS_2/sapphire (18.8 MW m^{-2} K^{-1}) compared to TBC for metal/sapphire interfaces from literature.[30–36] MTL_{Debye} is the maximum transmission limit in the Debye approximation (see Equation (3)). c) MD simulated average temperature profile for "bulk" MoS_2 (red diamonds) on crystalline Al_2O_3 (blue hexagons). The background shows the simulation structure and the atom positions corresponding to the overlaid temperature profile. The temperature difference at the interface is denoted by ΔT. d) Average temperature transients using the approach-to-equilibrium MD method for monolayer MoS_2 on both crystalline sapphire (c-Al_2O_3, blue line and left inset) and amorphous Al_2O_3 (a-Al_2O_3, green line and right inset). Dashed black lines represent the fit to Equation (S1) in the Supporting Information.

electronics with optimal thermal performance. For example, it may be important to consider a tradeoff between choosing more conductive crystalline substrates with lower TBC, and less conductive amorphous substrates with higher TBC. Detailed descriptions of the MD simulations and density of states figures can be found in the Supporting Information.

To further understand the origin of this low TBC from a phenomenological point of view, we consider the description of TBC based on the phonon irradiance and transmission coefficient.[6] In the maximum transmission limit (MTL), we can write the TBC in terms of the temperature derivative of the irradiance of the vibrationally weaker side. In the case of MoS_2/Al_2O_3, as for several metal/Al_2O_3 systems, the irradiance of Al_2O_3 is higher and therefore the TBC is limited by the vibrational properties of the MoS_2 film. Under the Debye approximation, the MTL of TBC is given by the following equation[6]

$$G_{\mathrm{MTL,\,Debye}} = \frac{1}{4} n_{\mathrm{a}} k_{\mathrm{B}} \sum_{\mathrm{p}} v_{\mathrm{s,p}} \tag{3}$$

where n_a is the atomic number density, k_B is the Boltzmann constant, and $v_{s,p}$ is the sound velocity of the branch with polarization p. In Figure 4b, we plot the experimentally measured TBC versus $G_{MTL,Debye}$ for MoS_2/c-Al_2O_3 and compare it with literature data for 15 different metals on the same substrate.[30–36] Assumed values for n_a and $v_{s,p}$ for all materials as well as compiled TBC data from literature are provided in Table S3 (Supporting Information). The observed correlation in Figure 4b indicates that one of the main factors causing low TBC at the TMD/Al_2O_3 interface is the small phonon frequencies and group velocities along the *c*-axis.

The second effect which can influence TBC is the interfacial bonding, which affects the transmission probabilities of phonons across the interface. A smaller work of adhesion correlates with lower transmission probabilities.[6,37] Weak bonding at the vdW interface between the layered material and sapphire substrate contributes towards a suppression of the TBC compared with strongly bonded metal/sapphire interfaces, while the range of measured TBCs for each material is likely due to variations in interface quality among the individual samples. We note that the quantitative calculation of TBC in layered materials requires a detailed modeling of the anisotropic dispersion and phonon-focusing effects;[38] however, the arguments presented above provide a reasonable starting point.

3. Conclusion

In summary, we have reported TBC values for several TMD/sapphire and graphite/sapphire interfaces near room temperature and presented a new method for measuring TBC in isolated single crystals, without the need to pattern any metal electrodes. We also find close agreement between measured values and NEMD simulations for the bulk MoS_2/sapphire interface TBC. This work opens possibilities for measuring nanoscale heat transport at buried interfaces and in confined geometries for any crystalline material. The high repetition rate (1.28 MHz) together with the brightness of the synchrotron allows for measurement of near-equilibrium dynamics associated with small temperature changes. Importantly, the material specificity offered by X-rays (e.g., see the clearly distinguished Bragg peaks in Figure 1b) will enable measurements of heat transport in complex crystalline heterostructures which find applications in high-power electronics, memory, energy harvesting, and optoelectronics. In general, this approach can be applied not only to single crystals, but also to polycrystalline materials, where the center-of-mass of a portion of the ring diffraction pattern can be tracked to measure thermal strain. This extends the range of possible materials to include small-grained metallic and semiconducting films deposited by techniques like evaporation and sputtering. The very large penetration depth of hard X-rays in most materials (≈4000 μm in diamond, ≈500 μm in Si, ≈20 μm in GaAs and GaN, and ≈15 μm in Cu at 15 keV) makes this approach very well suited for noninvasive thermal characterization of deeply buried interfaces. Furthermore, as this technique does not require microfabrication or deposition of additional transducer layers, it is ideal for in situ measurements of heat transport in operating electrical and electrochemical devices, including functional thermal materials.[39] Finally, the use of X-ray nanobeam diffraction can provide new insights into the dynamics of heat flow in locally heterogeneous, defect-rich materials.[40]

Supporting Information

Supporting Information is available from the Wiley Online Library or from the author.

Acknowledgements

C.N. and A.S. contributed equally to this work. This work was supported by the Department of Energy, Office of Science, Basic Energy Sciences, Materials Sciences and Engineering Division under Contract No. DE-AC02-76SF00515. Part of this work was performed at the Stanford Nano Shared Facilities (SNSF), supported by the National Science Foundation under award ECCS-1542152. C.N. acknowledges support from the NSF through a Graduate Research Fellowship (DGE-114747). This work was also supported by ASCENT, one of the six centers in JUMP, an SRC program sponsored by DARPA, and the Stanford SystemX Alliance. A.J.G. acknowledges partial support from an NDSEG Fellowship. The authors also thank Stanford University and the Stanford Research Computing Center (Sherlock cluster) for providing computational resources and support.

Conflict of Interest

The authors declare no conflict of interest.

Keywords

heterogeneous integration, thermal boundary conductance, time-resolved X-ray diffraction, transition metal dichalcogenides

Received: March 11, 2020
Revised: April 25, 2020
Published online: June 30, 2020

[1] A. Giri, P. E. Hopkins, *Adv. Funct. Mater.* **2019**, *30*, 1903857.
[2] Y. Zhao, Y. Cai, L. Zhang, B. Li, G. Zhang, J. T. L. Thong, *Adv. Funct. Mater.* **2020**, *30*, 1903929.
[3] D. G. Cahill, P. V Braun, G. Chen, D. R. Clarke, S. Fan, K. E. Goodson, P. Keblinski, W. P. King, G. D. Mahan, A. Majumdar, H. J. Maris, S. R. Phillpot, E. Pop, L. Shi, *Appl. Phys. Rev.* **2014**, *1*, 011305.
[4] A. Sood, E. Pop, M. Asheghi, K. E. Goodson, in *2018 17th IEEE Intersoc. Conf. Therm. Thermomechanical Phenom. Electron. Syst. (ITherm)*, IEEE, San Diego, CA, USA **2018**, pp. 1396–1402.
[5] A. Gaitonde, A. Nimmagadda, A. Marconnet, *J. Power Sources* **2017**, *343*, 431.
[6] C. Monachon, L. Weber, C. Dames, *Annu. Rev. Mater. Res.* **2016**, *46*, 433.
[7] P. E. Hopkins, L. M. Phinney, J. R. Serrano, T. E. Beechem, *Phys. Rev. B* **2010**, *82*, 085307.
[8] E. Yalon, Ö. B. Aslan, K. K. H. Smithe, C. J. McClellan, S. V. Suryavanshi, F. Xiong, A. Sood, C. M. Neumann, X. Xu, K. E. Goodson, T. F. Heinz, E. Pop, *ACS Appl. Mater. Interfaces* **2017**, *9*, 43013.
[9] A. J. Schmidt, K. C. Collins, A. J. Minnich, G. Chen, *J. Appl. Phys.* **2010**, *107*, 104907.
[10] M. Holler, M. Odstrcil, M. Guizar-sicairos, M. Lebugle, E. Müller, S. Finizio, G. Tinti, C. David, J. Zusman, W. Unglaub, O. Bunk, J. Raabe, A. F. J. Levi, G. Aeppli, *Nat. Electron.* **2019**, *2*, 464.
[11] M. M. S. Aly, M. Gao, G. Hills, C.-S. Lee, G. Pitner, M. M. Shulaker, T. F. Wu, M. Asheghi, J. Bokor, F. Franchetti, K. E. Goodson, C. Kozyrakis, I. Markov, K. Olukotun, L. Pileggi, E. Pop, J. Rabaey, C. Re, H.-S. P. Wong, S. Mitra, *IEEE Comput.* **2015**, *48*, 24.
[12] Z. Ong, M. Bae, *2D Mater.* **2019**, *6*, 032005.
[13] E. Yalon, C. J. McClellan, K. K. H. Smithe, M. Muñoz Rojo, R. L. Xu, S. V. Suryavanshi, A. J. Gabourie, C. M. Neumann, F. Xiong, A. B. Farimani, E. Pop, *Nano Lett.* **2017**, *17*, 3429.
[14] X. Gu, Y. Wei, X. Yin, B. Li, R. Yang, *Rev. Mod. Phys.* **2018**, *90*, 041002.
[15] J. Yang, E. Ziade, C. Maragliano, R. Crowder, X. Wang, M. Stefancich, M. Chiesa, A. K. Swan, A. J. Schmidt, *J. Appl. Phys.* **2014**, *116*, 023515.
[16] D. G. Cahill, *Rev. Sci. Instrum.* **1990**, *61*, 802.
[17] Y. Liu, Z. Ong, J. Wu, Y. Zhao, K. Watanabe, T. Taniguchi, D. Chi, G. Zhang, J. T. L. Thong, C.-W. Qiu, K. Hippalgaonkar, *Sci. Rep.* **2017**, *7*, 43886.
[18] S. Vaziri, E. Yalon, M. M. Rojo, S. V Suryavanshi, H. Zhang, C. J. Mcclellan, C. S. Bailey, K. K. H. Smithe, A. J. Gabourie, V. Chen, S. Deshmukh, L. Bendersky, A. V Davydov, E. Pop, *Sci. Adv.* **2019**, *5*, eaax1325.
[19] M. Kozina, T. Hu, J. S. Wittenberg, E. Szilagyi, M. Trigo, T. A. Miller, C. Uher, A. Damodaran, L. Martin, A. Mehta, J. Corbett, J. Safranek, D. A. Reis, A. M. Lindenberg, *Struct. Dyn.* **2014**, *1*, 034301.
[20] R. Shayduck, H. Navirian, W. Leitenberger, J. Goldshteyn, I. Vrejoui, M. Weinelt, P. Gaal, M. Herzog, C. von K. Schmising, M. Bargheer, *New J. Phys.* **2011**, *13*, 093032.
[21] E. M. Mannebach, C. Nyby, F. Ernst, Y. Zhou, J. Tolsma, Y. Li, M.-J. Sher, I.-C. Tung, H. Zhou, Q. Zhang, K. L. Seyler, G. Clark, Y. Lin, D. Zhu, J. M. Glownia, M. E. Kozina, S. Song, S. Nelson, A. Mehta, Y. Yu, A. Pant, O. B. Aslan, A. Raja, Y. Guo, A. DiChiara, W. Mao, L. Cao, S. Tongay, J. Sun, D. J. Singh, T. F. Heinz, X. Xu, A. H. MacDonald, E. Reed, H. Wen, A. M. Lindenberg, *Nano Lett.* **2017**, *17*, 7761.
[22] B. Krenzer, A. Janzen, P. Zhou, D. Von Der Linde, M. Horn-Von Hoegen, *New J. Phys.* **2006**, *8*, 190.
[23] A. Sood, F. Xiong, S. Chen, R. Cheaito, F. Lian, M. Asheghi, Y. Cui, D. Donadio, K. E. Goodson, E. Pop, *Nano Lett.* **2019**, *19*, 2434.
[24] S. Chen, A. Sood, E. Pop, K. E. Goodson, D. Donadio, *2D Mater.* **2019**, *6*, 025033.
[25] D. O. Lindroth, P. Erhart, *Phys. Rev. B* **2016**, *94*, 115205.
[26] H. Zhang, X. Chen, Y. D. Jho, A. J. Minnich, *Nano Lett.* **2016**, *16*, 1643.
[27] X. J. Yan, Y. Y. Lv, L. Li, X. Li, S. H. Yao, Y. Bin Chen, X. P. Liu, H. Lu, M. H. Lu, Y. F. Chen, *Appl. Phys. Lett.* **2017**, *110*, 211904.
[28] S. V. Suryavanshi, A. J. Gabourie, A. Barati Farimani, E. Pop, *J. Appl. Phys.* **2019**, *126*, 055107.
[29] C. J. Foss, Z. Aksamija, *2D Mater.* **2019**, *6*, 025019.
[30] R. J. Stoner, H. J. Maris, *Phys. Rev. B* **1993**, *48*, 16373.
[31] M. Jeong, J. P. Freedman, H. J. Liang, C. M. Chow, V. M. Sokalski, J. A. Bain, J. A. Malen, *Phys. Rev. Appl.* **2016**, *5*, 014009.
[32] J. P. Freedman, X. Yu, R. F. Davis, A. J. Gellman, J. A. Malen, *Phys. Rev. B* **2016**, *93*, 035309.
[33] P. E. Hopkins, R. N. Salaway, R. J. Stevens, P. M. Norris, *Int. J. Thermophys.* **2007**, *28*, 947.
[34] M. Blank, L. Weber, *J. Appl. Phys.* **2019**, *125*, 095302.
[35] R. Cheaito, J. T. Gaskins, M. E. Caplan, B. F. Donovan, B. M. Foley, A. Giri, J. C. Duda, C. J. Szwejkowski, C. Constantin, H. J. Brown-Shaklee, J. F. Ihlefeld, P. E. Hopkins, *Phys. Rev. B* **2015**, *91*, 035432.
[36] Y. M. Sheu, M. Trigo, Y. J. Chien, C. Uher, D. A. Arms, E. R. Peterson, D. A. Walko, E. C. Landahl, J. Chen, S. Ghimire, D. A. Reis, *Solid State Commun.* **2011**, *151*, 826.
[37] R. Prasher, *Appl. Phys. Lett.* **2009**, *94*, 041905.
[38] Z. Chen, Z. Wei, Y. Chen, C. Dames, *Phys. Rev. B* **2013**, *87*, 125426.
[39] A. Sood, F. Xiong, S. Chen, H. Wang, D. Selli, J. Zhang, C. J. McClellan, J. Sun, D. Donadio, Y. Cui, E. Pop, K. E. Goodson, *Nat. Commun.* **2018**, *9*, 4510.
[40] A. Sood, R. Cheaito, T. Bai, H. Kwon, Y. Wang, C. Li, L. Yates, T. Bougher, S. Graham, M. Asheghi, M. Goorsky, K. E. Goodson, *Nano Lett.* **2018**, *18*, 3466.

ADVANCED FUNCTIONAL MATERIALS

Supporting Information

for *Adv. Funct. Mater.*, DOI: 10.1002/adfm.202002282

Visualizing Energy Transfer at Buried Interfaces in Layered Materials Using Picosecond X-Rays

*Clara Nyby, Aditya Sood, Peter Zalden, Alexander J. Gabourie, Philipp Muscher, Daniel Rhodes, Ehren Mannebach, Jeff Corbett, Apurva Mehta, Eric Pop, Tony F. Heinz, and Aaron M. Lindenberg**

Supporting Information

Visualizing energy transfer at buried interfaces in layered materials using picosecond x-rays

*Clara Nyby†, Aditya Sood†, Peter Zalden, Alexander J. Gabourie, Philipp Muscher, Daniel Rhodes, Ehren Mannebach, Jeff Corbett, Apurva Mehta, Eric Pop, Tony F. Heinz, Aaron M. Lindenberg**

† These authors contributed equally to this work

Molecular dynamics simulations

To compare with experimental results, we compute the thermal boundary conductance (TBC) using molecular dynamics (MD). All MD simulations are run using the LAMMPS package.[1] We model MoS_2 with the Stillinger-Weber (SW) potential parameterized by Jiang *et al*.[2] and Al_2O_3 with the Vashishta potential.[3] Interactions between MoS_2 and Al_2O_3 atoms, as well as interactions between MoS_2 layers were modeled by the Lennard-Jones (LJ) potential. LJ parameters are from the universal force field[4] and parameters for atom pairs of different type are calculated using Lorentz-Berthelot mixing rules. The LJ parameters are presented below in Table S2. For all simulations, we use a time step of 1 fs. This timestep is confirmed to maintain constant system energy when running in the constant atom number, volume, and energy ensemble (NVE).

We compute the TBC at two different MoS_2 thickness extremes: 'bulk' and single-layer. For bulk-like MoS_2, we use the non-equilibrium MD (NEMD) method to extract the TBC. Experimentally, bulk out-of-plane thermal properties are not observed until thicknesses > 500 nm in MoS_2.[5] Here we use 20 layers of MoS_2 (~13 nm thick) as an approximation of bulk behavior but mostly to serve as a structure comparatively much thicker than single-layer MoS_2. The 20-layer MoS_2 stack is placed on top of 16 nm of crystalline Al_2O_3 (c-Al_2O_3) with an interfacial area of 4.9 × 5.7 nm^2 (structure in background of Fig. 4c in main text). Periodic boundary conditions are applied in the *x* and *y* directions but not in the *z* direction. Initially, this system is equilibrated to 300 K in the constant volume and temperature ensemble (NVT) for 10 ps. Using the top three layers of MoS_2 as a heater (320 K) and the bottommost 2015 atoms (~0.7 nm) of c-Al_2O_3 as a heat sink (280 K), we apply a temperature gradient of 40 K over the structure. We apply this temperature gradient for 1 ns to reach a steady-state heat current. We continue for an additional 2 ns, but now record temperatures and the heat current. The averages, as

well as the errors, of the TBC extractions are computed over ten independent simulations. The resulting average temperature profile can be seen in Fig. 4c of the main text.

The TBC is extracted using the following expression based on Fourier's law: $J = G\Delta T$, where J is the heat flux, G is the TBC, and ΔT is the temperature difference between the two materials at the interface. For our simulations, we had an average heat flux of J = 300.24 ± 12.24 MWm^{-2} and an average ΔT = 16.16 ± 0.34 K (Fig. 4c in the main text) yielding a TBC of G = 18.58 ± 0.81 $MWm^{-2}K^{-1}$. This number represents the TBC between bulk MoS_2 and c-Al_2O_3, in the range of measured values for MoS_2 (8-28 $MWm^{-2}K^{-1}$; as seen in Fig. 4a of the main text).

To better understand the TBC of our bulk-like MD structure, we compute the phonon density of states (PDOS) of both bulk MoS_2 and c-Al_2O_3 by taking the Fourier transform of the velocity autocorrelation function. The result is plotted in Fig. S1. The flexural acoustic phonons[6] (from out-of-plane atomic motion) are found below 5 THz but, in this range, it is difficult to determine to what degree the Al_2O_3 substrate couples to the MoS_2. However, there are significant MoS_2 peaks, corresponding to optical modes, that overlap with the Al_2O_3 phonon DOS. This overlap likely couples MoS_2 to Al_2O_3 well around 10 – 14 THz.

Next, we investigate the TBC of single-layer MoS_2 on Al_2O_3. To compute the TBC, we use the approach-to-equilibrium molecular dynamics (AEMD) method used recently.[7] The NEMD method is not appropriate because a thermostat would be required at the interface, interfering with any calculation of ΔT. For these simulations we use a 5.4 nm thick block of c-Al_2O_3 and a single layer of MoS_2 on top. Additionally, we created an amorphous Al_2O_3 (a-Al_2O_3) block to examine if substrate defects could change the TBC. The interfacial area is identical to that in the NEMD approach. Larger interface areas and thicker Al_2O_3 were not found to affect the results. The crystalline and amorphous Al_2O_3 structures are shown in the inset of Fig. 4d in the main text.

The simulation procedure is as follows: First, we run at constant pressure and temperature (NPT) at 0 atmosphere and 300 K until the system volume oscillations die out (10 ps). Next, we stabilize the entire system's temperature at 300 K for an additional 10 ps in the NVT ensemble. We then take 25 ps to ramp the temperature of the MoS_2 to 500 K (while keeping the Al_2O_3 at 300 K). This state is held for 10 ps to stabilize the temperature again. Finally, we remove all thermostats, place the system in the NVE ensemble, and let it equilibrate. During the equilibration process, we monitor the temperature of both MoS_2 and Al_2O_3.

We model the system and the temperature transient as a resistive-capacitive (RC) thermal circuit (Fig. S2a). The expression for the temperature difference between MoS_2 and Al_2O_3, i.e. $\Delta T = T_{MoS_2} - T_{Al_2O_3}$, can be written as:[7]

$$\Delta T = \Delta T_0 e^{-\left(\frac{1}{m_{MoS_2} C_{MoS_2}} + \frac{1}{m_{Al_2O_3} C_{Al_2O_3}}\right) AGt} \quad \text{(S1)}$$

where m and C are the respective mass and specific heat per unit mass, A is the area of the interface, G is the TBC, and t is the time. Since we start the thermal relaxation process with T_{MoS_2} = 500 K and $T_{Al_2O_3}$ = 300 K, the initial difference is ΔT_0 = 200 K. Fitting this expression to Eq. S1 from ten independent MD simulations allows us to extract the TBC between the two materials. Both ΔT and the fit to Eq. S1 for crystalline and amorphous Al_2O_3 are shown in Fig. 4d in the main text.

For the c-Al_2O_3 substrate (inset of Fig. 4d in the main text), the extracted TBC is 15.3 ± 0.3 $MWm^{-2}K^{-1}$. Comparing directly to the NEMD-extracted TBC, we find that single-layer MoS_2 TBC is 18% lower. Calculations and experimental measurements show the out-of-plane thermal conductivity of MoS_2 to be decreasing with decreasing thickness.[5] Thus, while a single-layer of MoS_2 represents an extreme with regards to thickness and its out-of-plane thermal transport may not behave similarly to a bulk MoS_2 crystal, we expect the TBC of MoS_2 on c-Al_2O_3 to decrease with thickness. Heat-carrying vibrational modes incident on the interface, present in the NEMD structure, will either have their mean free paths restricted by the thickness of single-layer MoS_2 or simply not exist as their wavelengths are larger than MoS_2 is thick. With respect to this work, there are sources of error which likely artificially reduce the difference between single-layer and bulk TBC. The NEMD approach, which has ~13 nm of MoS_2, only approximates bulk out-of-plane thermal transport. Recent experimental results[5] show that the out-of-plane thermal conductivity does not saturate until an MoS_2 thickness > 500 nm. Based on our explaination above of the relationship between thermal conductivity and TBC, we expect the NEMD TBC extraction to be an underestimate of the true bulk MoS_2 on c-sapphire TBC. We may also be overestimating the room-temperature TBC using the AEMD method as we are fitting to a single temperature transient curve that spans ~200 K. We find the TBC to decrease when we fit Eq. S1 to larger time ranges (e.g. 100 ps, 200 ps, 300 ps, etc.). However, the noise in ΔT increases with time, making TBC extractions over large time ranges less reliable. Balancing these factors, we chose to fit the first 100 ps of ΔT calculations to Eq. S1; however, if we place any trust into the noisy extractions over large time ranges, a TBC ~10% smaller may be possible. The cumulative effect of these errors gives the impression that single-layer and bulk MoS_2 on c-Al_2O_3 TBCs are closer to each other than in reality. Still, it is unlikely that there is a strong dependence of TBC on MoS_2 thickness as an increase in thickness by a factor of 20 does not yield even a doubling of the TBC in our simulations.

Finally, the a-Al_2O_3 substrate (inset of Fig. 4d in the main text) results in a TBC of 18.9 ± 0.5 $MWm^{-2}K^{-1}$. These calculations represent the disordered limit for pure Al_2O_3 and show that a more disordered Al_2O_3 substrate yields a higher TBC consistent with the conclusions of a recent study.[8] An increase in TBC from a crystalline AlN to an amorphous SiO_2 substrate was also seen in previous work[7] and, while that work compared different substrate materials in conjunction with a change in crystallinity, we find their TBC trend and their accompanying analysis can be extended to our case as well. Figs. S2b and S2c shows the PDOS of crystalline and amorphous Al_2O_3 combined with single-layer MoS_2. Since the same number of atoms are in c-Al_2O_3 as in a-Al_2O_3, both substrates have the same number of modes; however, the peaks of the PDOS of a-Al_2O_3 are broadened and their height reduced,

'flattening' out the distribution. This leads to a greater PDOS overlap than in the c-Al_2O_3 case. MoS_2 phonons relevant to the TBC will have more vibrational states to couple with in a-Al_2O_3 compared to phonon modes in c-Al_2O_3, resulting in a higher TBC.

Sample preparation

For the $Mo_{0.93}W_{0.07}Te_2$ sample, single crystals were synthesized through a chemical vapor transport technique using iodine or $TeCl_4$ as the transport agent. Samples were held at 750 °C with a 100 °C temperature gradient for 1 week, then subsequently cooled over 3 days to 400 °C and removed from the furnace. Each growth commonly yielded crystals of both structure types (Td and 2H). Stoichiometry was determined by energy dispersive X−ray spectroscopy (EDS) analysis through a field-emission scanning electron microscope (FEI Nova 400). All other bulk crystals were purchased from the commercial suppliers HQgraphene or 2Dsemiconductors.

The bulk crystals were exfoliated on the sapphire substrates using a polydimethysiloxane (PDMS) stamp method. The thickness of individual flakes was measured using a Park XE-70 scanning probe microscope (See Figure S3).

Material	**Fit Input**				
	Thickness (nm)	**κ_z ($Wm^{-1}K^{-1}$)**	**Heat capacity C_v ($Jg^{-1}K^{-1}$)**	**Density (gcm^{-3})**	**Penetration depth L_p (nm)**
MoS_2	33	1.19	0.40[9]	5.06	36[10]
	43	1.35			
	52	1.49			
	130	2.25			
	200	2.67			

$MoSe_2$	39	0.89	0.28[11]	6.96	19[10]
	180	1.77			
$MoTe_2$	30	0.65	0.22[12]	7.70	26
	360	1.89			
WSe_2	103	0.48	0.21[13]	9.32	26[10]
	185	0.67			
WS_2	106	0.49	0.26[14]	7.50	30[10]
$MoWTe_2$	33	0.42	0.22[12]	7.70	26
	156	0.84			
Graphite	200	3.4	0.72[15]	2.15	28[16]

Table S1. Input parameters for finite element (FE) simulations.

Atom Pair	ϵ (meV)	σ (Å)
Mo-Mo	2.43	2.72
S-S	11.88	3.59
Mo-Al	7.29	3.36
Mo-O	2.51	2.92
S-Al	16.13	3.80
S-O	5.56	3.36

Table S2. Parameters for the LJ potential defined for all atomic pairs in the MD simulations.

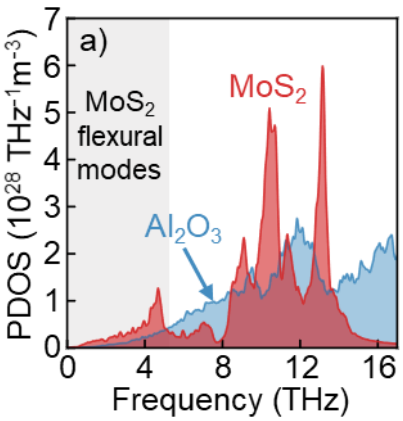

Figure S1. (a) The PDOS of both 'bulk' MoS_2 and Al_2O_3 structures from the inset of Fig. 4c in the main text. The gray shading highlights the frequencies corresponding to the flexural MoS_2 phonons.

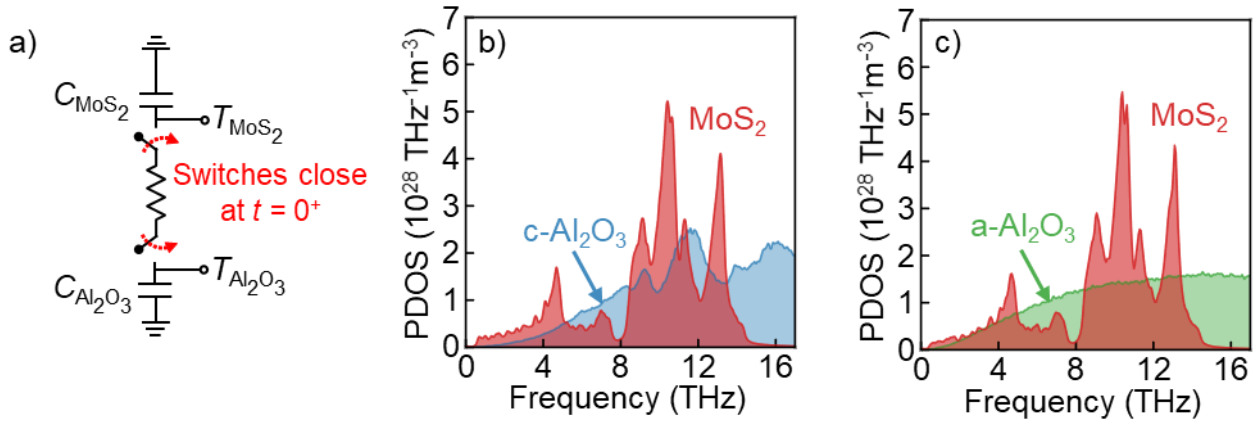

Figure S2. (a) The equivalent RC thermal circuit that Eq. S1 is derived from. This circuit models the temperature behavior in Fig. 4d in the main text. (b), (c) PDOS of single-layer MoS_2 on a c-Al_2O_3 and an a-Al_2O_3 substrate, respectively.

Metal	n_a **(atoms/m^3)**	v_s **LA (m/s)**	v_s **TA (m/s)**	**MTL$_{Debye}$ (MWm^{-2}K^{-1})**	**TBC on Sapphire (MWm^{-2}K^{-1})**
Al	6.02E+28	6360	3130	2621.048	180[17], 185[18], 311[19], 160[20]
Bi	2.82E+28	2180	430	296.0527	19.5[21]
Cr	8.28E+28	6850	3980	4229.347	390[22], 349[20]
Cu	8.56E+28	4760	2300	2764.769	180[22], 197[23], 175[20]
Au	5.9E+28	3280	1190	1151.657	45[17], 65[22], 57[20],
Pb	3.29E+28	2160	700	403.6209	55[17],
Mo	6.4E+28	6250	3350	2857.685	216[20]
Ni	9.08E+28	5810	3080	3750.142	283[20]
Pd	6.82E+28	4540	1900	1960.907	167[23], 126[19], 152[20]
Pt	6.64E+28	4080	1690	1708.277	180[18], 85[19], 106[20]
Ag	5.85E+28	3640	1690	1417.484	77[20],
Ta	5.45E+28	4100	2900	1863.014	141[20]
Ti	5.66E+28	6070	3125	2404.15	218[17], 324[19],
W	6.31E+28	5180	2870	2378.908	131[20]
Ir	7.05E+28	5380	3050	2794.08	147[20]
MoS_2	1.9E+28	3300	2000	479.4783	8 - 28 [This work]

Table S3. Values for atomic number density n_a, sound speed v_s for longitudinal acoustic (LA) and transverse acoustic (TA) branches, and computed thermal boundary conductance (TBC) in the maximum transmission limit assuming Debye dispersion, MTL$_{Debye}$. Also provided are experimental data from literature for TBC measurements between these materials and sapphire.

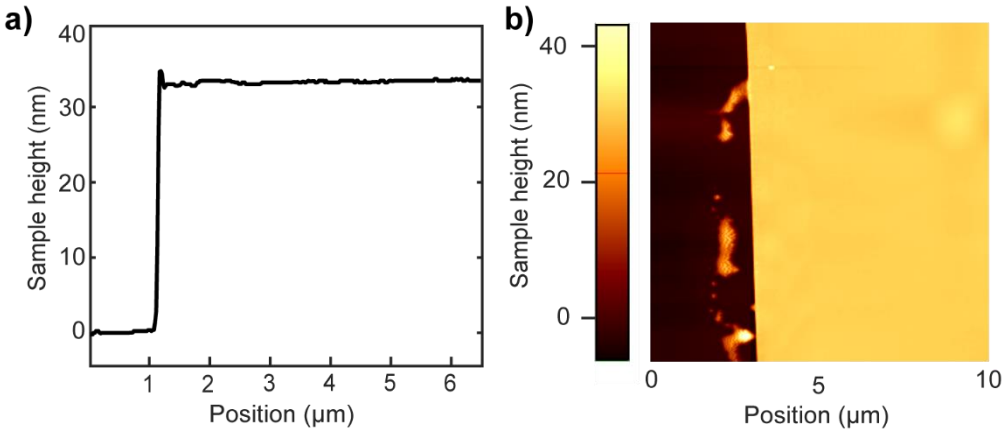

Figure S3. AFM topography of a 33 nm thick MoS_2 flake on sapphire substrate, (a) line plot and (b) image.

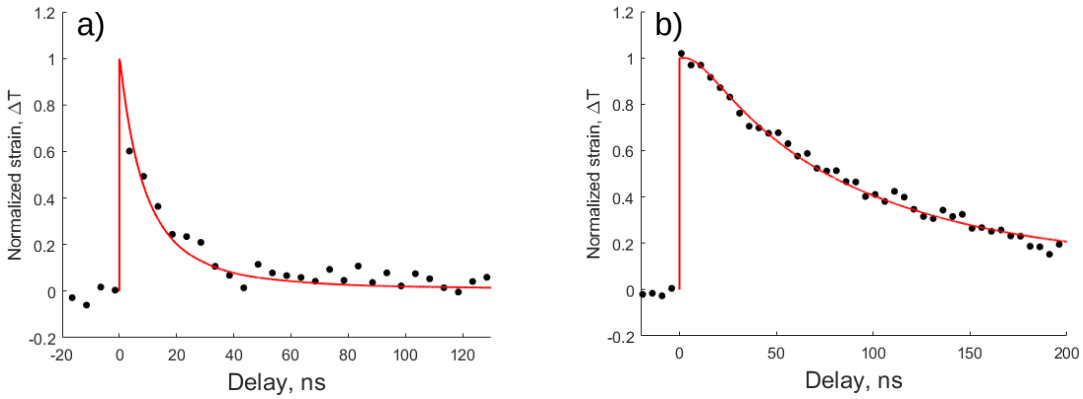

Figure S4. Strain response in $MoTe_2$ a) 30 nm thick flake and b) 360 nm thick flake

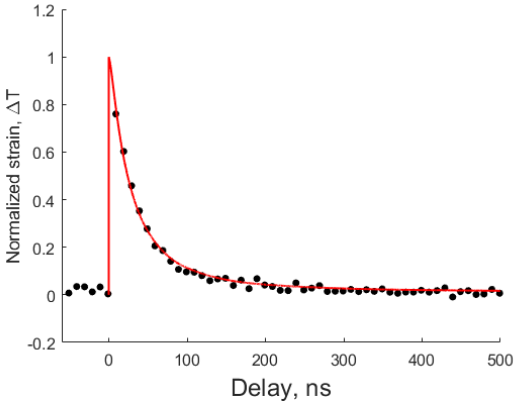

Figure S5. Strain response in a 106 nm thick flake of WS_2

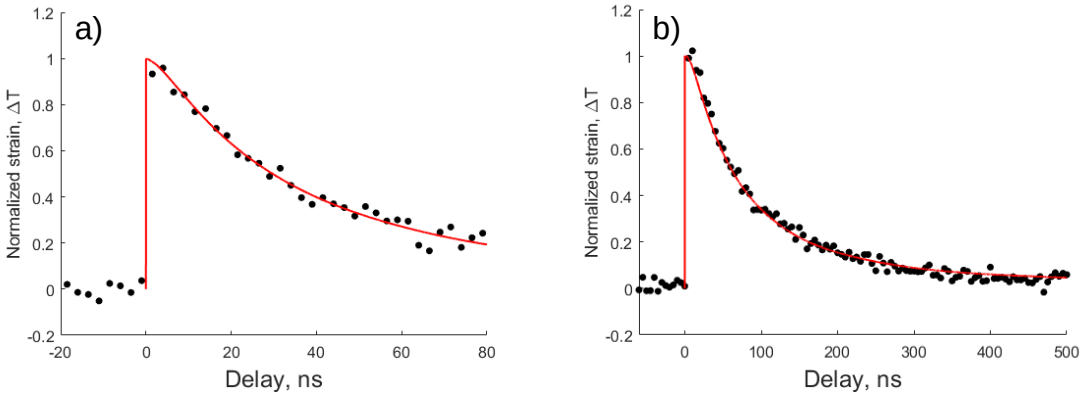

Figure S6. Strain response in WSe_2 a) 103 nm thick flake and b) 185 nm thick flake

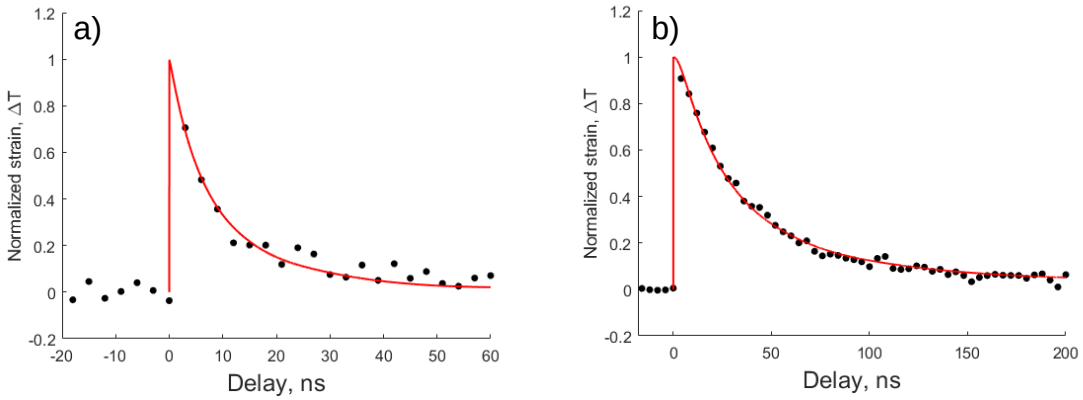

Figure S7. Strain response in $Mo_{0.93}W_{0.07}Te_2$ a) 33 nm thick flake and b) 156 nm thick flake

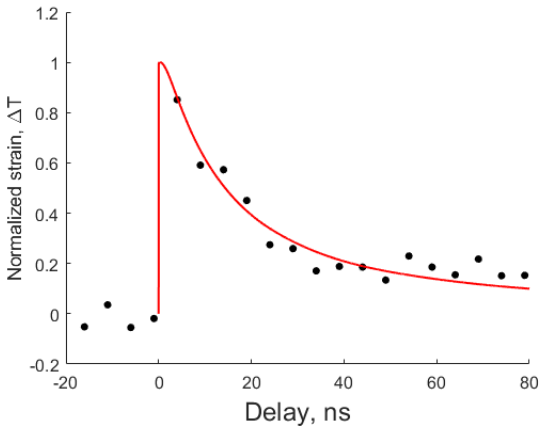

Figure S8. Strain response in a 200 nm thick flake of graphite.

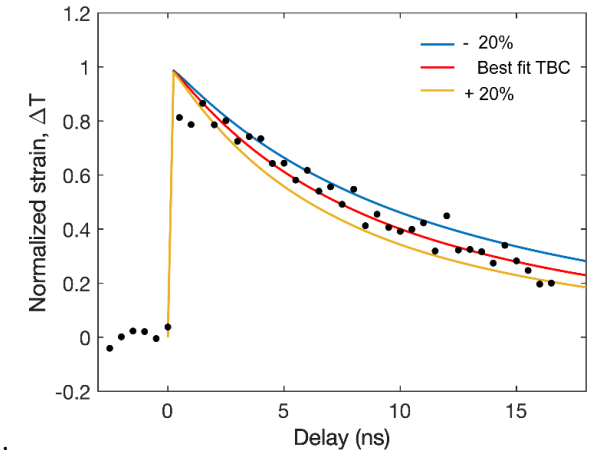

.

Figure S9. Strain response in a 39 nm flake of $MoSe_2$ (same as Fig. 3c) showing measurement sensitivity by perturbing the best-fit result by ± 20 %.

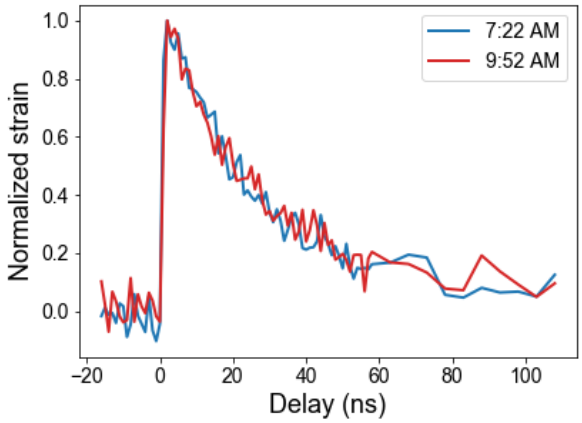

Figure S10: Strain response in 130 flake of MoS_2, showing repeatability of the measurement. Each curve shows an average of 3 scans of the time window, with the measurements taken 2.5 hours apart.

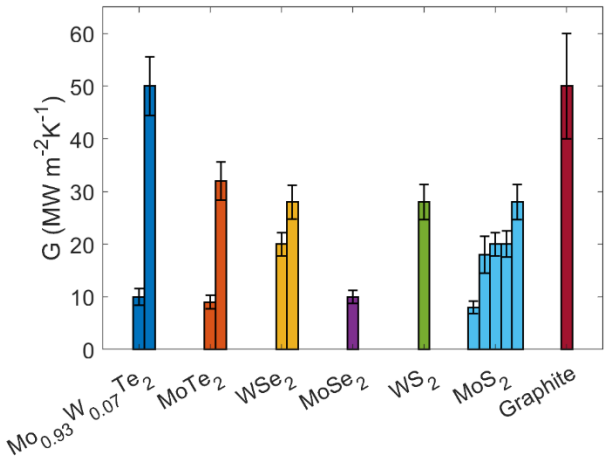

Figure S11: Summary of measured TBC data, ordered based on the calculated MTL values.

References for Supplemental Information:

[1] S. Plimpton, *J. Comput. Phys.* **1995**, *117*, 1.

[2] J. W. Jiang, H. S. Park, T. Rabczuk, *J. Appl. Phys.* **2013**, *114*, 064307.

[3] P. Vashishta, R. K. Kalia, A. Nakano, J. P. Rino, *J. Appl. Phys.* **2008**, *103*, 083504.

[4] A. K. Rappé, C. J. Casewit, K. S. Colwell, W. A. Goddard, W. M. Skiff, *J. Am. Chem. Soc.* **1992**,

114, 10024.

[5] A. Sood, F. Xiong, S. Chen, R. Cheaito, F. Lian, M. Asheghi, Y. Cui, D. Donadio, K. E. Goodson, E. Pop, *Nano Lett.* **2019**, *19*, 2434.

[6] A. Molina-Sánchez, L. Wirtz, *Phys. Rev. B* **2011**, *84*, 155413.

[7] S. V. Suryavanshi, A. J. Gabourie, A. Barati Farimani, E. Pop, *J. Appl. Phys.* **2019**, *126*, 055107.

[8] C. J. Foss, Z. Aksamija, *2D Mater.* **2019**, *6*, 025019.

[9] L. S. Volovik, V. V. Fesenko, A. S. Bolgar, S. V. Drozdova, L. A. Klochkov, V. F. Primachenko, *Sov. Powder Metall. Met. Ceram.* **1978**, *17*, 697.

[10] Y. Li, A. Chernikov, X. Zhang, A. Rigosi, H. M. Hill, A. M. Van Der Zande, D. A. Chenet, E. M. Shih, J. Hone, T. F. Heinz, *Phys. Rev. B* **2014**, *90*, 205422.

[11] A. Olin, *Chemical Thermodynamics of Selenium, Volume 1*, **2005**.

[12] H. L. Kiwia, E. F. Westrum, *J. Chem. Thermodyn.* **1975**, *7*, 523.

[13] A. S. Bolgar, Z. A. Trofimova, A. A. Yanaki, *Powder Metall. Met. Ceram.* **1990**, *29*, 382.

[14] P. A. G. O'Hare, W. N. Hubbard, G. K. Johnson, H. E. Flotow, *J. Chem. Thermodyn.* **1984**, *16*, 45.

[15] E. Pop, V. Varshney, A. K. Roy, *MRS Bull.* **2012**, *37*, 1273.

[16] A. B. Kuzmenko, E. Van Heumen, F. Carbone, D. Van Der Marel, *Phys. Rev. Lett.* **2008**, *100*, 117401.

[17] R. J. Stoner, H. J. Maris, *Phys. Rev. B* **1993**, *48*, 16373.

[18] P. E. Hopkins, R. N. Salaway, R. J. Stevens, P. M. Norris, *Int. J. Thermophys.* **2007**, *28*, 947.

[19] R. Cheaito, J. T. Gaskins, M. E. Caplan, B. F. Donovan, B. M. Foley, A. Giri, J. C. Duda, C. J. Szwejkowski, C. Constantin, H. J. Brown-Shaklee, J. F. Ihlefeld, P. E. Hopkins, *Phys. Rev. B* **2015**, *91*, 035432.

[20] M. Blank, L. Weber, *J. Appl. Phys.* **2019**, *125*, 095302.

[21] Y. M. Sheu, M. Trigo, Y. J. Chien, C. Uher, D. A. Arms, E. R. Peterson, D. A. Walko, E. C. Landahl, J. Chen, S. Ghimire, D. A. Reis, *Solid State Commun.* **2011**, *151*, 826.

[22] M. Jeong, J. P. Freedman, H. J. Liang, C. M. Chow, V. M. Sokalski, J. A. Bain, J. A. Malen, *Phys. Rev. Appl.* **2016**, *5*, 014009.

[23] J. P. Freedman, X. Yu, R. F. Davis, A. J. Gellman, J. A. Malen, *Phys. Rev. B* **2016**, *93*, 035309.